



Novel photoactivation promoted light-driven CO₂ reduction by CH₄ on Ni/CeO₂ nanocomposite with high light-to-fuel efficiency and enhanced stability



Qian Zhang, Mingyang Mao, Yuanzhi Li*, Yi Yang, Hui Huang, Zhongkai Jiang, Qianqian Hu, Shaowen Wu, Xiujuan Zhao

State Key Laboratory of Silicate Materials for Architectures (Wuhan University of Technology), 122 Luoshi Road, Wuhan 430070, PR China

ARTICLE INFO

Keywords:
Photocatalytic
Photothermocatalytic
CO₂ reduction by CH₄
Ni/CeO₂ nanocomposite
Light-to-fuel efficiency

ABSTRACT

The catalytic CO₂ reduction by CH₄ to synthesize fuels of CO and H₂ (CRM) supplies a prospective technology to address the global warming effect caused by greenhouse gas of CO₂. Due to its highly endothermic characteristics, CRM can only proceed at high reaction temperature, resulting in excessive energy consumption and quick catalyst deactivation due to serious carbon. Herein, we report a nanocomposite of Ni/CeO₂ that exhibits high catalytic activity and good stability with focalized UV-vis-Infrared (UV-vis-IR) illumination without applying any other heater. It generates high production rates of H₂ and CO (6.53 and 6.27 mmol min⁻¹ g⁻¹), its light-to-fuel efficiency (η) is up to 11.1%. Ni/CeO₂ shows efficient catalytic activity with 11.0% of η even with focalized Vis-IR illumination of wavelengths above 690 nm. Based on the experimental evidences, it is found that the highly effective catalytic performance of Ni/CeO₂ under the focalized illumination originates from the efficient light-driven thermocatalytic CRM. It is discovered for the first time that a synergistic effect among Ni nanoparticles and CeO₂ remarkably facilitates the catalytic durability of the Ni/CeO₂ nanocomposite. We delve into the origin of the synergistic effect by combining evidences of XRD, TEM, TG-MS, FTIR, and isotopic labelling: The lattice oxygen of CeO₂ in Ni/CeO₂ participates in the oxidation of C* species formed on Ni nanoparticles via the migration at the Ni/CeO₂ interface, thus significantly enhancing the catalytic stability due to the inhibition of carbon deposition. It is found that the solar-light-driven thermocatalytic activity of Ni/CeO₂ is considerably improved by a novel photoactivation, which is quite different from the conventional photocatalysis on semiconductor photocatalysts. The novel photoactivation is theoretically revealed by DFT calculation: The irradiation obviously decreases the activation energy of the dominant steps of the C and CH oxidations for CRM on metallic Ni, thus considerably improving the catalytic activity of metallic Ni.

1. Introduction

Carbon dioxide (CO₂) is enormously emitted from various processes related to combustion of fossil fuels. CO₂ as greenhouse gas (GHG) causes global warming effect, which is one of major global environmental problems. The rational exploitation of renewable solar energy to control GHG emission has received comprehensive focus due to its significant importance. CO₂ as a feedstock has been transformed to valuable chemicals and/or fuels by employing solar energy. The reported works involve solar thermochemical splitting of CO₂ [1,2], photoelectrochemical or photocatalytic CO₂ reduction by water [3–20], photothermocatalytic CO₂ reduction by H₂ [21,22], solar-light-driven (SLD) CO₂ reduction by CH₄ [23–31], and so on. Among them, SLD thermocatalytic CO₂

reduction by CH₄ (CRM: CH₄ + CO₂ = 2CO + 2H₂) is especially promising as it not only provides an effective strategy to convert CO₂ to CO and H₂ as chemical feedstock or fuels, but also provides an exciting solution to realize the conversion between solar energy and chemical energy by utilizing the extremely endothermic characteristics of CRM ($\Delta H_{298} = 247 \text{ kJ mol}^{-1}$, $\Delta G_{298} = 170.5 \text{ kJ mol}^{-1}$) [25–32]. However, to realize the SLD thermocatalytic CRM, the catalyst should have not only high thermocatalytic activity and good thermocatalytic stability, but also have strong absorption and efficient photothermal conversion across a wide region of solar spectra up to infrared region. It is very difficult and great challenging to design such a SLD thermocatalyst for CRM that could simultaneously satisfy the above requirements.

From the view of thermodynamics, only at high reaction

* Corresponding author.

E-mail address: liyuanzhi66@hotmail.com (Y. Li).

temperature (generally over 700 °C) is CRM able to proceed. The high reaction temperature causes severe carbon deposit and sintering of the catalyst, resulting in rapid catalyst deactivation [31,33–35]. The supported precious metals (e.g. Rh, Pt, Ru) were reported to exhibit the best initial catalytic activity for SLD CRM. But they are easily deactivated [19–24]. Ni-based catalysts as potential alternatives to the expensive precious metal catalysts were also reported to exhibit good initial catalytic activities for SLD CRM, but they were more easily deactivated due to more serious carbon deposition than the precious metal catalysts [26]. Thermodynamic analysis reveals that carbon deposition, derived from CH₄ decomposition (CH₄ = 2H₂ + C, ΔH_{298K} = 75 kJ mol⁻¹) and CO disproportionation (2CO = CO₂ + C, ΔH_{298K} = -172 kJ mol⁻¹), is thermodynamically favorable at reaction temperatures below 1000 °C [33]. This means that the carbon deposition is thermodynamically unavoidable. Consequently, exploiting novel Ni-based catalysts that could kinetically restrain carbon deposition is urgent and significant for the SLD thermocatalytic CRM.

Herein, we prepared a Ni/CeO₂ nanocomposite by a facile method. The Ni/CeO₂ nanocomposite demonstrates high catalytic activity and superior stability for CRM under localized UV-vis-IR illumination without applying any other heater. Its production rates of H₂ and CO are 6.53 and 6.27 mmol min⁻¹ g⁻¹, and its light-to-fuel efficiency is up to 11.1%. We reveal that the effective catalytic performance of Ni/CeO₂ under the localized illumination derives from the efficient light-driven thermocatalytic CRM. It is found for the first time that a synergistic effect between Ni nanoparticles and CeO₂ remarkably facilitates the catalytic stability of the Ni/CeO₂ nanocomposite due to the inhibition of carbon deposition. We delve into the origin of the synergistic effect by combining evidences of XRD, TEM, TG-MS, FTIR, and isotope labelling. A novel photoactivation is found to considerably improve the solar-light-driven thermocatalytic activity of Ni/CeO₂. We put insight into the novel photoactivation by DFT calculations.

2. Experimental

2.1. Preparation

The sample of Ni/CeO₂ nanocomposite was prepared in accordance to the following procedure: 14.474 g Ce(NO₃)₃·6H₂O and 3.8772 g Ni(NO₃)₂·6H₂O were dissolved into 20 mL distilled water under stirring. 9.8065 g citric acid (C₆H₈O₇·6H₂O) was dissolved into 50 mL distilled water under stirring. The citric acid aqueous solution was added dropwise to the Ce(NO₃)₃ and Ni(NO₃)₂ solution under stirring. The solution in a beaker covered by polyethylene film was aged in a water bath at 60 °C for 3 h, and then kept at 80 °C for 24 h in an electric oven. The obtained powder was ground in a mortar. 1.0 g of the powder was heated to 400 °C in a muffle furnace at a 1.6 °C min⁻¹ heating rate, and kept at the temperature for 4 h. The obtained NiO/CeO₂ sample was ground in a mortar. The NiO/CeO₂ powder in a quartz tubular reactor, which was put in an electrical tubular furnace, was heated to 700 °C, kept at 700 °C for 1 h, and finally cooled to room temperature in a flow of 10.2 vol% CH₄, 10.3 vol% CO₂, and Ar (balance gas) at a 40 mL min⁻¹ flow rate. The obtained sample is denoted as Ni/CeO₂. The Ni/Ce molar ratio in the Ni/CeO₂ nanocomposite is 0.4, corresponding to a Ni loading amount of 12.0 wt%.

The pure CeO₂ sample was prepared by a procedure, the same as that of the above Ni/CeO₂ nanocomposite except for no addition of Ni(NO₃)₂·6H₂O.

The Ni/CeO₂ nanocomposites with different Ni/Ce molar ratios of 0.05, 0.20, and 0.50 (corresponding to the Ni loading amounts of 1.7, 6.4, 14.6 wt%, respectively) were prepared by a procedure, the same as that of the above Ni/CeO₂ nanocomposite except for using different amounts of Ni(NO₃)₂·6H₂O and citric acid. The Ni/CeO₂ nanocomposites obtained are denoted as Ni/CeO₂-0.05, Ni/CeO₂-0.20, and Ni/CeO₂-0.5. Their amounts of Ni(NO₃)₂·6H₂O used are 0.4847, 1.9386, and 4.8465 g, while the amounts of citric acid used are 7.005, 7.3549,

and 10.507 g, respectively. For the preparation of all the samples of Ni/CeO₂ nanocomposites, the molar ratio of citric acid and metal salts (Ce(NO₃)₃ and Ni(NO₃)₂) is 0.70.

The referenced sample of Ni/SiO₂ was prepared in accordance to the following procedure: 1.3527 g Ni(NO₃)₂·6H₂O was dissolved into 20 mL distilled water. 2.0 g silica was added to the Ni(NO₃)₂ aqueous solution under magnetic stirring. 3.4 g NaOH aqueous solution (9.9 wt%) was dropped to the suspension under vigorous magnetic stirring. The resultant slurry was filtered, washed with distilled water, and dried at 180 °C for 12 h. The NiO/SiO₂ sample obtained was heated to 700 °C, and kept at the temperature for 1 h in a quartz tube reactor in a flow of 10.2 vol% CH₄, 10.3 vol% CO₂, and Ar (balance gas) with a 40 mL min⁻¹ flow rate. The sample obtained is denoted as Ni/SiO₂. The Ni amount in Ni/SiO₂ is 12.0 wt%.

2.2. Characterization

XRD patterns of the sample were acquired on a RigakuDmax X-ray diffractometer equipped with Cu K α radiation. TEM images were recorded by a JEM-ARM200 F machine. BET surface area was examined by N₂ adsorption at 77.15 K on ASAP2020. The XPS spectra were acquire by an X-ray photoelectron spectrometer (ESCALAB 250Xi) using Mg K α radiation. Thermogravimetric/mass spectrometry (TG-MS) characterization was carried out by the STA449F3 thermal analyser combined with mass spectrometer. UV-vis-IR spectra were acquired on a Lambda 750S spectrophotometer. Raman spectra were obtained on a Renishaw in Via Raman microscope using 514.5 nm excitation.

2.3. Photothermocatalytic activity

The catalytic activity of the samples for CRM was carried out on a reactor schematically illustrated in Scheme S1. A 500 W Xe lamp with emission across the whole solar spectra (200–2400 nm) [36] was used as light source. 0.0500 g of the sample was put in a sample holder of thermal insulation aluminum silicate cotton that was placed in the reactor. The illumination from the Xe lamp was focalized on the sample through the quartz window. The temperature of the sample with the focalized illumination was measured by a thermocouple that was contacted closely to the sample. A gas stream of 9.8 vol% CH₄, 10.0 vol% CO₂, and Ar (balance gas), adjusted by a S49-31/MT mass flow meter, was fed to the reactor at a 122.0 mL min⁻¹ flow rate. A soap bubble flow meter was used to measure the gas flow rate. The effluents from the reactor were analyzed through a sampling valve by a gas chromatograph (GC-9560). A TDX-01 packed column was used for the separation of effluents. A thermal conductivity detector was used for analyzing H₂, a methane convector was used for converting CO₂ and CO to CH₄, and a flame ionization detector was used for analyzing CH₄. An Newport 1918-R optical power meter connected to a Newport 818P-001-12 thermopile sensor was used to measure the illumination power focalized into the reactor. The optical power meter was calibrated by AM 1.5 global sunlight (Newport).

The power of the focalized UV-vis-IR illumination was 7.13 W. The focalized illumination area (diameter, 0.5 cm) is 0.19625 cm², so that the illumination intensity is 363.4 kW m⁻² (corresponding to 363.4 suns). To measure the catalytic activity of Ni/CeO₂ for CRM with focalized Vis-IR illumination, a long-wave pass cutoff filter of 420, 560, or 690 nm was put between the Xe lamp and the quartz window (Scheme 1S). The powers of the focalized Vis-IR illumination with wavelengths above 420, 560, and 690 nm are 5.99, 5.19, and 4.03 W, respectively. The corresponding illumination intensities are 305.0, 264.3, and 205.3 kW m⁻², respectively.

2.4. Photocatalytic activity

The photocatalytic performance of the Ni/CeO₂ sample for CRM at near room temperature in the reactor. 0.0500 g of Ni/CeO₂ on a glass

flake was put on the bottom of the reactor. The reactor was put in an ice-water bath to ensure near room temperature with the Xe lamp illumination. The illumination intensity is 4.7 kW m^{-2} . The other procedure is identical to that for measuring the photothermocatalytic activity.

2.5. Thermocatalytic activity

The thermocatalytic performance of Ni/CeO₂ for CRM at different temperatures was tested in a quartz tubular reactor on a online gas-phase reaction apparatus (WFS-2015). 0.0500 g of Ni/CeO₂ mixed with 0.5 g quartz particles was put in the reactor. A thermocouple was contacted closely to the Ni/CeO₂ sample to detect the temperature in the reactor. A gas stream of 10.2 vol% CH₄, 10.3 vol% CO₂, and Ar (balance gas) was constantly fed to the reactor at a 29.6 mL min^{-1} flow rate.

2.6. Catalytic activity with focalized illumination or in the dark at different temperatures

The catalytic activity of the Ni/CeO₂ sample with the focalized illumination or in the dark at different temperatures was measured in the quartz tube reactor for measuring thermocatalytic activity as described above. 0.0050 g of Ni/CeO₂ was put on a quartz wool support in the middle of the quartz reactor. In the case, a quartz window was connected to the end of the quartz tube reactor. The illumination from the Xe lamp was focalized on the sample in the quartz tube reactor through the quartz window. A gas stream of 10.2 vol% CH₄, 10.3 vol% CO₂, and Ar (balance gas) was constantly fed into the reactor at a 10 mL min^{-1} flow rate.

2.7. Isotope labeling of thermocatalytic CRM

Isotope labeling experiment of thermocatalytic CRM on Ni/CeO₂ was conducted on a setup as illustrated in Scheme S3 in accordance to the procedure as follows. A quartz tubular reactor was connected through a micro pump to a quartz tubular FTIR cell with two CaF₂ windows that was placed in a Nicolet-6700 infrared spectrometer. 0.0500 g NiO/CeO₂ was placed in the quartz tubular reactor. The system was pre-purged with high purity N₂. NiO/CeO₂ was heated to 700°C in a flow of 10.2 vol% CH₄, 10.3 vol% CO₂, and Ar (balance gas) at a 30 mL min^{-1} flow rate, and kept at 700°C for 1 h to pre-reduce NiO/CeO₂ to Ni/CeO₂. Then, the system was purged by high purity N₂. 20 mL of ¹²CH₄, 10 mL of ¹²C¹⁸O₂ (Aldrich), and 270 mL of high purity N₂ (balance gas) were fed into the system by the corresponding gas bags. The micro pump was turned on, and FTIR spectra of the reactants and products from the reaction of ¹²CH₄ and ¹²C¹⁸O₂ on Ni/CeO₂ were recorded on Nicolet-6700 infrared spectrometer.

2.8. DFT calculations

Density functional theory (DFT) calculations were conducted by utilizing Perdew–Burke–Ernzerhof (PBE) GGA-exchange correlation functional and projected augmented wave (PAW) approach [37,38] in a VASP 5.3 Vienna Ab Initio Simulation Package. A slab of Ni₃₆ consisting of four Ni layers with a 3×3 {111} surface cell and a cubic structure (JCPDS 65–2865) was constructed as a model of metallic Ni. The space between neighbouring {111} surfaces of the Ni₃₆ slab was 1.0 nm . A $3 \times 3 \times 1$ Monkhorst-Pack k-point mesh was utilized for summation over the Brillouin zone. For the structure optimization, the convergence criteria for the electronic relaxation and ionic relaxation were 10^{-4} eV and $10^{-3} \text{ eV } \text{\AA}^{-1}$, respectively. Dimer method was utilized to seek the transition states [31,39]. The saddle point of the transition state was optimized by a force-based conjugate gradient method [40] until the rotational force was less than $0.01 \text{ eV } \text{\AA}^{-1}$ and the total energy was converged to within $1 \times 10^{-7} \text{ eV atom}^{-1}$.

3. Results and discussion

3.1. Characterization

The sample of Ni/CeO₂ nanocomposite was prepared by the reaction among Ce(NO₃)₃, Ni(NO₃)₂, and citric acid, followed by the pre-reduction in a feed stream of CH₄ and CO₂ at 700°C (see Experimental). XRD reveals that Ni/CeO₂ is a mixture of metallic Ni (JCPDS 65-2865) and CeO₂ with pure cubic fluorite structure (JCPDS 89-8436) (Fig. S1). The average crystal size of CeO₂ and metallic Ni nanoparticles in Ni/CeO₂, calculated in accordance to the Scherrer formula ($L = 0.89\lambda/\beta\cos\theta$), are 24.7 and 16.4 nm, respectively. TEM images with the element mapping show that Ni nanoparticles are generally uniformly distributed on CeO₂ (Fig. 1A–D). TEM image shows that CeO₂ and Ni nanoparticle in Ni/CeO₂ are closely contacted (Fig. 1E). HRTEM image shows that Ni nanocrystal with lattice spacings of {111} facets is closely contacted to the surrounding CeO₂ nanocrystals with lattice spacings of {111} facets and different orientations. N₂ adsorption measurement demonstrates that Ni/CeO₂ has a BET surface area of $50.7 \text{ m}^2 \text{ g}^{-1}$.

The valence states of Ni in Ni/CeO₂ are obtained by fitting its Ni2p3/2 spectra (Fig. S2A). The peak at 852.3 eV with its satellite at 858.3 eV is assigned to Ni_{2p3/2} of Ni⁰. The peak at 855.5 eV with its satellite at 861.0 eV is attributed to Ni_{2p3/2} of Ni²⁺ [41]. The Ni⁰/Ni²⁺ molar ratio is estimated by XPS to be 0.26. The existence of a considerable amount of Ni²⁺ species is ascribed to the surface oxidation of Ni nanoparticles during the exposure of Ni/CeO₂ in air. The valence states of Ce in Ni/CeO₂ are obtained by fitting its Ce3d spectra (Fig. S2B). The peaks of v, v'', v''' and u, u'', u''' are attributed to Ce3d_{5/2} and Ce3d_{3/2} of Ce⁴⁺ species. The peaks of v₀, v' and u₀, u' are attributed to Ce3d_{5/2} and Ce3d_{3/2} of Ce³⁺ species [42,43]. The molar ratio of Ce³⁺/(Ce³⁺ + Ce⁴⁺) is estimated to be 0.21.

3.2. Photothermocatalytic performance

The photothermocatalytic performance of the samples for CRM was evaluated on a flow cylinder-shaped stainless steel reactor with focalized illumination from a 500 W Xe lamp (which has emission across the whole solar spectra) without applying any other heater (Scheme S1). A gas stream of 9.8 vol% CH₄, 10.0 vol% CO₂, and Ar (balance gas) was constantly fed into the reactor at a $120.0 \text{ mL min}^{-1}$ flow rate. Ni/CeO₂ displays efficient catalytic performance under the focalized UV-vis-IR illumination. As shown in Fig. 2A, its reaction rates of CH₄ ($r_{\text{CH}4}$) and CO₂ (r_{CO_2}) are 2.99 and $3.23 \text{ mmol min}^{-1} \text{ g}^{-1}$, respectively. Its production rates of H₂ (r_{H_2}) and CO (r_{CO}) are 6.53 and $6.27 \text{ mmol min}^{-1} \text{ g}^{-1}$, respectively (Fig. 2B). The light-to-fuel efficiency (η) for CRM on Ni/CeO₂ is calculated according to the following equation [1] S1.

$$\eta = (r_{\text{H}_2} \times \Delta_c H^\circ_{\text{H}_2} + r_{\text{CO}} \times \Delta_c H^\circ_{\text{CO}} - r_{\text{CH}4} \times \Delta_c H^\circ_{\text{CH}4}) / P_{\text{illumination}}$$

$$R = F \cdot C_i$$

$\Delta_c H^\circ_{\text{H}_2}$, $\Delta_c H^\circ_{\text{CO}}$, and $\Delta_c H^\circ_{\text{CH}4}$ are the standard heats of combustion (25°C) or higher heating values for H₂, CO, and CH₄, respectively (Note: CO₂ is not a fuel, and its $\Delta_c H^\circ$ is 0), r is the molar production rate of products (r_{H_2} , r_{CO}) or the molar reaction rate of reactants ($r_{\text{CH}4}$, r_{CO_2}), F is the flow rate of the feed stream, C_i is the concentration of reactants and products, and $P_{\text{illumination}}$ is the power of the illumination focalized into the reactor.

The calculated η value of Ni/CeO₂ with focalized UV-vis-IR illumination is 11.1% (Fig. 2C).

The thermodynamic maximum η_{max} value, limited by the Carnot and solar absorption efficiencies, was calculated in accordance to the formula: [2]

$$\eta_{\text{max}} = [1 - \sigma \times T_{\text{H}}^{-4} / (I_{\text{DNi}} \times C)] \times [1 - T_{\text{L}} / T_{\text{H}}]$$

where C is the concentration ratio of solar flux. I_{DNi} is the direct normal

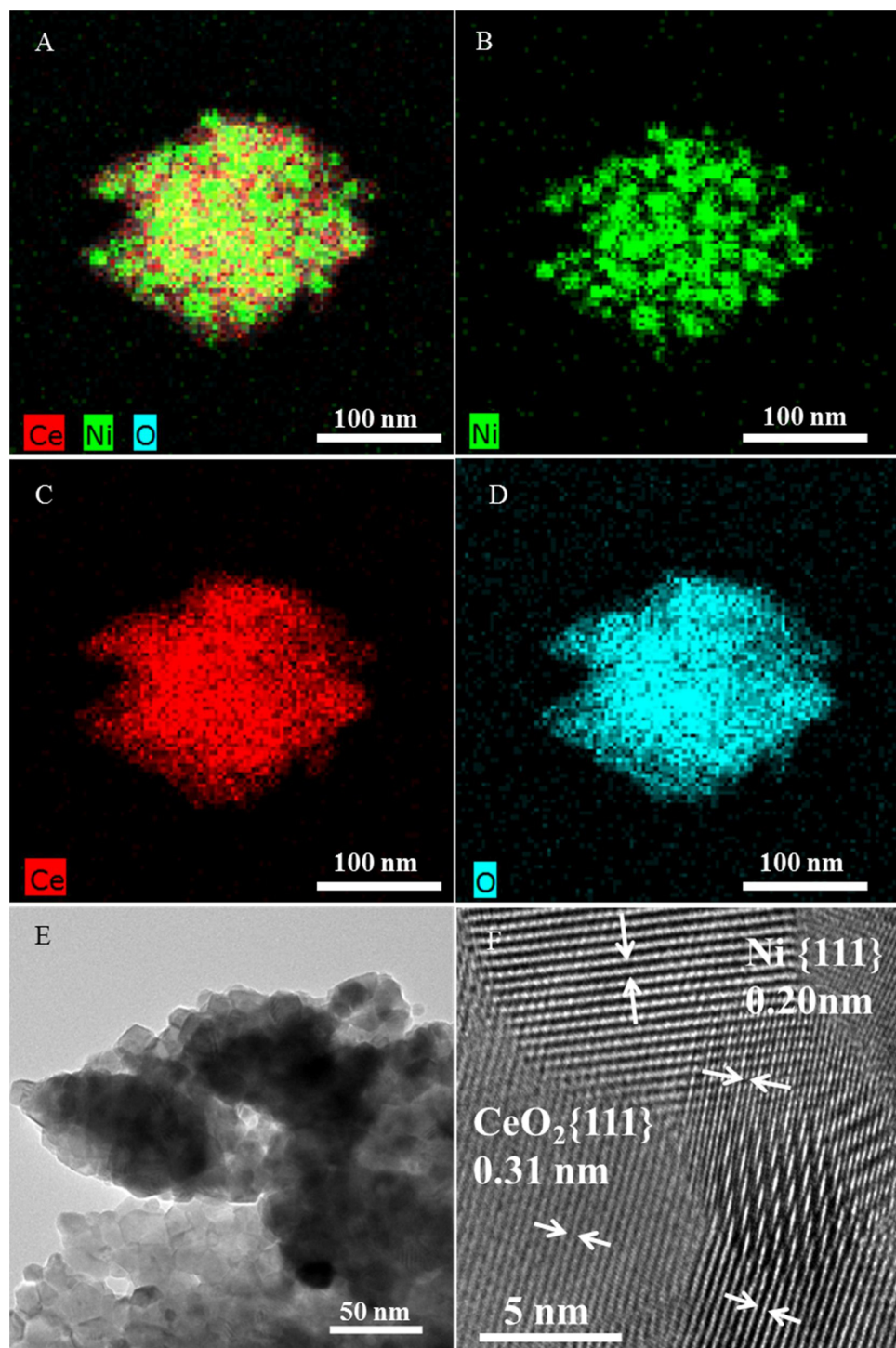


Fig. 1. TEM images with element mapping (A–D), TEM (E), HRTEM (F) of the Ni/CeO₂ sample.

solar illumination (1000 W m^{-2}). σ is the Stefan–Boltzmann constant. T_L and T_H are the low and high temperatures of the equal Carnot heat engine. In the present case, $C = 363.4$ (see SI) and T_L (25 °C). With focalized UV–vis–IR illumination, the temperature of Ni/CeO₂ is 807 °C (T_{H_2} , as discussed later). The calculated η_{\max} value is 56.0%, far exceeding the measured η value (11.1%).

The photothermocatalytic activity of the pure CeO₂ sample, which was prepared by a procedure, the same as that of Ni/CeO₂ except for no adding Ni(NO₃)₂, was evaluated with focalized UV–vis–IR illumination under the conditions identical to those of the Ni/CeO₂ sample. The pure CeO₂ sample has pure cubic fluorite structure with average crystal size

of 8.4 nm (Fig. S1) and morphology of closely contacted nanoparticles (Fig. S3). It has a BET surface area of $110.0 \text{ m}^2 \text{ g}^{-1}$. Its r_{H_2} and r_{CO} values are 0.17 and $0.81 \text{ mmol min}^{-1} \text{ g}^{-1}$, respectively, 37.6 and 7.8 times lower than the corresponding those of Ni/CeO₂ (Fig. 2B). The η value of CeO₂ is 0.5% (Fig. 2C). The result shows that the Ni/CeO₂ nanocomposite formation remarkably enhances the catalytic activity and Ni nanocrystals in Ni/CeO₂ play a significant role in the catalytic enhancement.

TiO₂ is a widely used photocatalyst that has very good photocatalytic activity for many reactions including CO₂ reduction by CH₄ [18]. For comparison, the photocatalytic activity of TiO₂ (P25) was

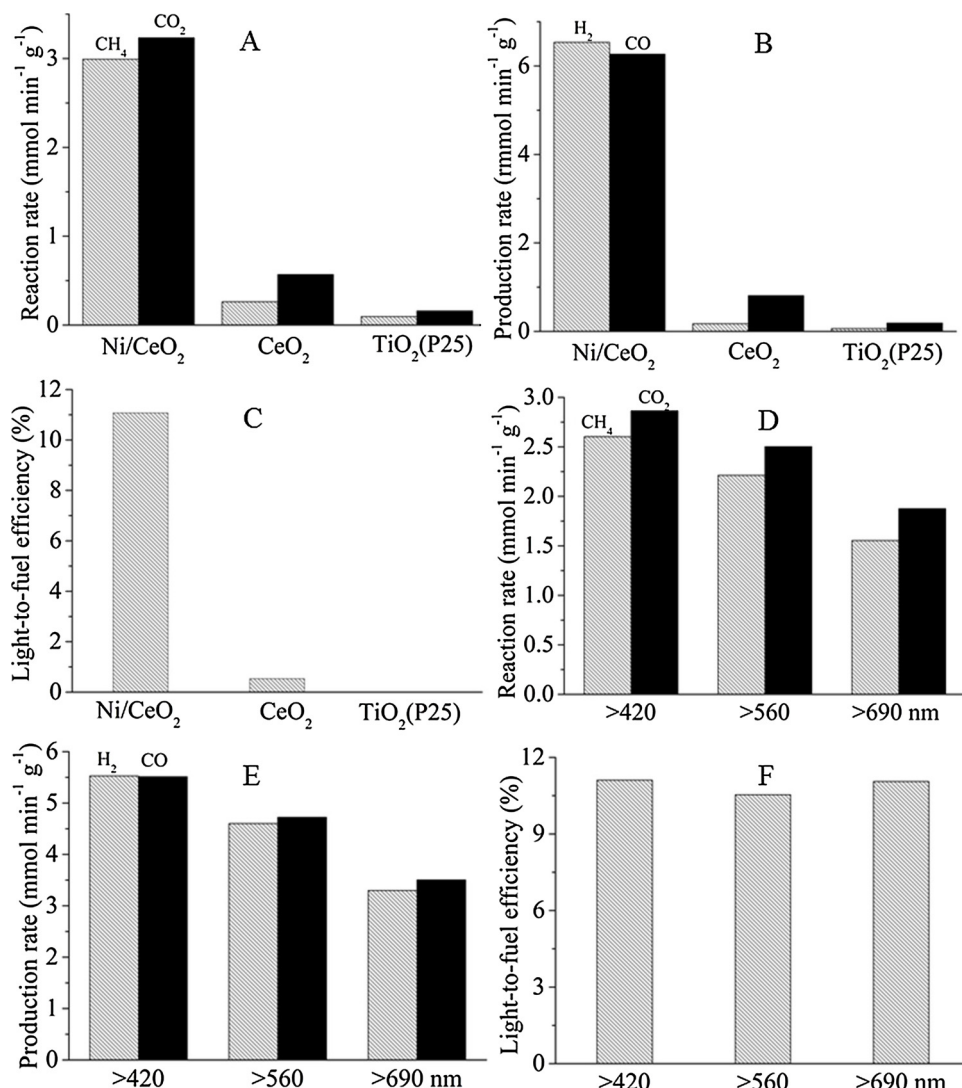


Fig. 2. The reaction rates of CH₄ and CO₂ (A), production rates of H₂ and CO (B), and light-to-fuel efficiency (C) of the samples with focalized UV-vis-IR illumination. The reaction rates of CH₄ and CO₂ (D), production rates H₂ and CO (E), and light-to-fuel efficiency (F) of Ni/CeO₂ with focalized Vis-IR illumination.

evaluated with focalized UV-vis-IR illumination. The r_{H_2} and r_{CO} of TiO₂ (P25) are only 0.063 and 0.188 mmol min⁻¹ g⁻¹, respectively (Fig. 2B). Its η value is inappreciable. Compared to TiO₂ (P25), the r_{H_2} and r_{CO} of Ni/CeO₂ are enhanced by 104.5 and 33.3 times, respectively.

The catalytic activity of Ni/CeO₂ with focalized Vis-IR illumination was also evaluated. Ni/CeO₂ presents considerably efficient catalytic activity with focalized Vis-IR illumination of wavelengths above 420 nm. The r_{H_2} and r_{CO} of Ni/CeO₂ are 5.51 and 5.51 mmol min⁻¹ g⁻¹, respectively (Fig. 2E). Its η value is up to 11.1% (Fig. 2F). With focalized Vis-IR illumination of wavelengths above 560 nm, the r_{H_2} and r_{CO} values of Ni/CeO₂ are 4.6 and 4.72 mmol min⁻¹ g⁻¹, respectively, and the η value is 10.6%. Even with focalized Vis-IR illumination of wavelengths above 690 nm, Ni/CeO₂ still exhibits good catalytic activity with high r_{H_2} and r_{CO} values (3.29 and 3.50 mmol min⁻¹ g⁻¹) and high η value (11.0%).

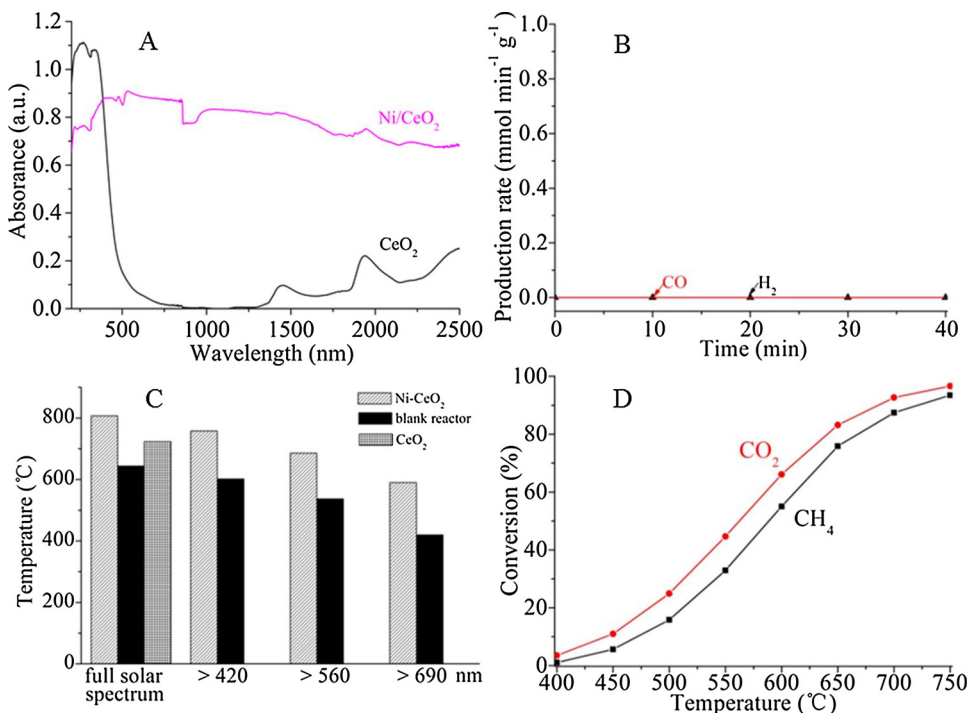
3.3. Mechanism: SLD thermocatalytic CRM

To demystify why Ni/CeO₂ possesses catalytic activity with focalized UV-vis-IR and Vis-IR illumination, the diffusive reflectance absorption spectra of the Ni/CeO₂ sample were recorded. Ni/CeO₂ displays strong absorption across the whole solar spectra (from 240 to 2400 nm) (Fig. 3A). The strong absorption below ~480 nm is ascribed

to the absorption of CeO₂ with 3.1 eV band gap (398 nm) [44,45]. This is evidenced by the fact that the pure CeO₂ sample has strong absorption below ~480 nm (Fig. 3A). The obvious red shift of its absorption edge is attributed to the existence of Ce³⁺ in the CeO₂ sample [44,45], which is proved by XPS data (Fig. S2B). Ni/CeO₂ exhibits strong broad absorption from ~480 to 2400 nm owing to surface plasmon absorption of Ni nanoparticles [31,32,46].

To verify whether the optical absorption of Ni/CeO₂ causes photocatalytic activity for CRM as CeO₂ is an n-type semiconductor photocatalyst, the photocatalytic activity of Ni/CeO₂ for CRM at near room temperature with UV-vis-IR illumination from the 500 W Xe lamp was measured. No detectable CO and H₂ are produced, indicating that Ni/CeO₂ has no photocatalytic activity for CRM (Fig. 3B). This indicates that the high catalytic activity of Ni/CeO₂ with focalized illumination (Fig. 2) derives from a light-driven thermocatalytic CRM:

With focalized illumination from the Xe lamp, the surface temperature of Ni/CeO₂ increases. The thermocatalytic CRM reaction occurs on condition that the temperature rises over the light-off temperature for thermocatalytic CRM on Ni/CeO₂ ($T_{\text{light-off}}$). To affirm the SLD thermocatalysis, we recorded the surface temperature of Ni/CeO₂ under the conditions identical to those of measuring the photo-thermocatalytic activity (Fig. 2). With focalized UV-vis-IR illumination, the surface temperature of Ni/CeO₂ speedily reaches to an equilibrium



temperature (T_{eq}) of 807 °C (Fig. 3C). The high T_{eq} value is attributed to the IR heating effect of the localized illumination as well as the photothermal conversion owing to the strong optical absorption of Ni/CeO₂. As shown in Fig. 3C, the temperature of the sample holder surface in the absence of the catalyst rapidly increases to a high T_{eq} value (644 °C) under localized UV-vis-IR illumination. This shows that the IR heating effect of the localized illumination play a major role in the temperature elevation of Ni/CeO₂ upon the localized UV-vis-IR illumination. The photothermal conversion of Ni/CeO₂ in the UV-vis region below ~480 nm is mainly ascribed to the heat generated by the recombination of electrons/holes in CeO₂ (Fig. 3A), evidenced by fact that the T_{eq} value (723 °C) of CeO₂ is higher than that of the sample holder surface with localized UV-vis-IR illumination (644 °C, Fig. 3C). The photothermal conversion of Ni/CeO₂ in the Vis-IR region above ~480 nm is mainly ascribed to the heat generated by the recombination of electrons/holes in Ni nanoparticles due to their strong surface plasmon absorption (Fig. 3A). This is confirmed by measuring the T_{eq} values of Ni/CeO₂ and the sample holder surface with localized Vis-IR illumination (Fig. 3C), because in these cases, the temperature increase caused by the photothermal conversion of CeO₂ is low due to its low absorption in the Vis-IR region above 480 nm. With localized Vis-IR illumination of wavelengths above 420, 560, or 690 nm, the T_{eq} value of Ni/CeO₂ is 758, 686, or 590 °C, respectively, which is higher than the corresponding value of the sample holder surface in the absence of the catalyst (602, 537, 420 °C, respectively). The photothermal conversion efficiency (η_{ptc}) of Ni/CeO₂ was measured (SI). The η_{ptc} value of Ni/CeO₂ with localized UV-vis-IR illumination is 23.4%. The η_{ptc} value of Ni/CeO₂ with localized Vis-IR illumination of wavelengths above 420, 560, or 690 nm is 26.2%, 26.4%, or 27.7%, respectively. The η_{ptc} value of Ni/CeO₂ with localized UV-vis-IR illumination lower than that with localized Vis-IR illumination indicates that the Vis-IR photothermal conversion of Ni/CeO₂ is more efficient than its UV photothermal conversion.

To verify if the IR heating effect of the localized illumination and the photothermal conversion are able to trigger the thermocatalytic CRM on Ni/CeO₂, we measured its thermocatalytic activity for CRM in the dark without the illumination at different temperatures. As shown in Fig. 3D, when the temperature reaches to 400 °C ($T_{light-off} = 400$ °C), CRM on Ni/CeO₂ starts to take place. With increasing the temperature

Fig. 3. Diffuse reflectance absorption spectra of the CeO₂ and Ni/CeO₂ samples (A). The time course of H₂ and CO production rates of the Ni/CeO₂ sample for CRM under the UV-vis-IR illumination at near room temperature (B). The T_{eq} values of the Ni/CeO₂ and CeO₂ samples, and the sample holder surface without the catalyst under the localized illumination (C). The thermocatalytic activity of the Ni/CeO₂ sample for CRM in the dark without the illumination at different temperatures (D).

from 450 to 700 °C, the thermocatalytic performance is remarkably facilitated. When the temperature reaches at 700 °C, the conversions of CH₄ and CO₂ are to 87.5% and 92.7%, respectively. Its temperatures at the CO₂ conversion of 50% and 90% (T_{50} and T_{90}) are 562 and 686 °C, respectively. All the T_{eq} values of Ni/CeO₂ with the localized UV-vis-IR and Vis-IR illumination (Fig. 3C) are higher than the $T_{light-off}$ value. Therefore, the SLD thermocatalytic CRM on Ni/CeO₂ is able to proceed.

As the photothermocatalytic CRM on Ni/CeO₂ under the localized illumination follows the SLD thermocatalysis, the thermocatalytic activity plays an important role in the photothermocatalytic activity. To search for the Ni/CeO₂ nanocomposite with the optimum catalytic activity, the Ni/CeO₂ nanocomposites with the different Ni/Ce molar ratios of 0.05, 0.20, and 0.50 were prepared by a procedure, the same as that of the above Ni/CeO₂ sample with the Ni/Ce molar ratio of 0.4. Their thermocatalytic activity was measured (Figs. S4 and S5). Among the Ni/CeO₂ nanocomposites, the Ni/CeO₂-0.05 has the lowest thermocatalytic activity. Its T_{50} and T_{90} values are 658 and > 750 °C, respectively. Increasing the Ni/Ce molar ratio to 0.20 causes a considerable increase in the thermocatalytic activity. The T_{50} and T_{90} values of Ni/CeO₂-0.2 decreases to 589 and 700 °C, respectively. By increasing the Ni/Ce molar ratio to 0.4, Ni/CeO₂ has the optimum thermocatalytic activity with the lowest T_{50} and T_{90} values (562 and 686 °C) (Fig. 3D). Further increasing the Ni/Ce molar ratio to 0.5 causes a reduction in the thermocatalytic activity. The T_{50} and T_{90} values of Ni/CeO₂-0.5 increase to 582 and 699 °C, respectively.

3.4. Catalytic stability and synergistic effect

The catalyst stability at high reaction temperature is important for the practical application of the catalytic CRM as the deactivation due to the carbon deposition is thermodynamically unavoidable [30–35]. To show if Ni/CeO₂ is catalytically stable for CRM, its catalytic durability was evaluated under the localized UV-vis-IR illumination. In this case, a stream of 9.7 vol% CH₄, 9.8 vol% CO₂, and Ar (balance gas) was constantly fed into the reactor at a 122.4 mL min⁻¹ flow rate. Ni/CeO₂ shows good durability (Fig. 4A). After the localized illumination for 100 h, only a slight decline in its r_{CH_4} and r_{CO_2} values (7.6% and 8.0%) is detected. As discussed above, Ni nanocrystals in Ni/CeO₂ serve as main catalytic active components, and CeO₂ also has catalytic activity

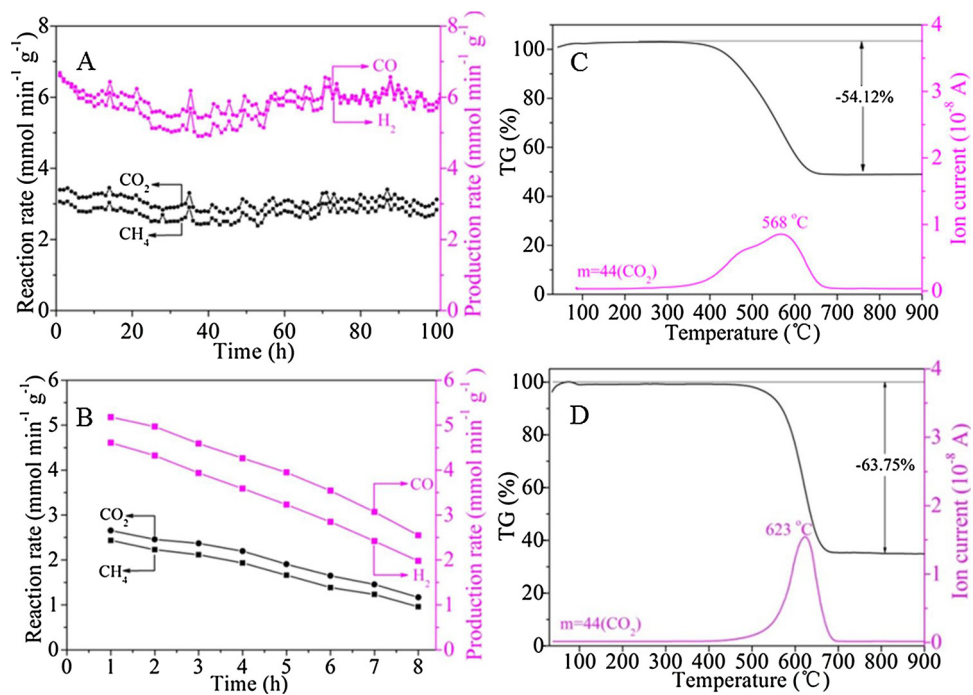


Fig. 4. The time course of the reaction and production rates for Ni/CeO₂ (A) and Ni/SiO₂ (B) with the focalized UV-vis-IR illumination. TG-MS profiles for the used Ni/CeO₂ (C) and Ni/SiO₂ (D) samples after the durability tests.

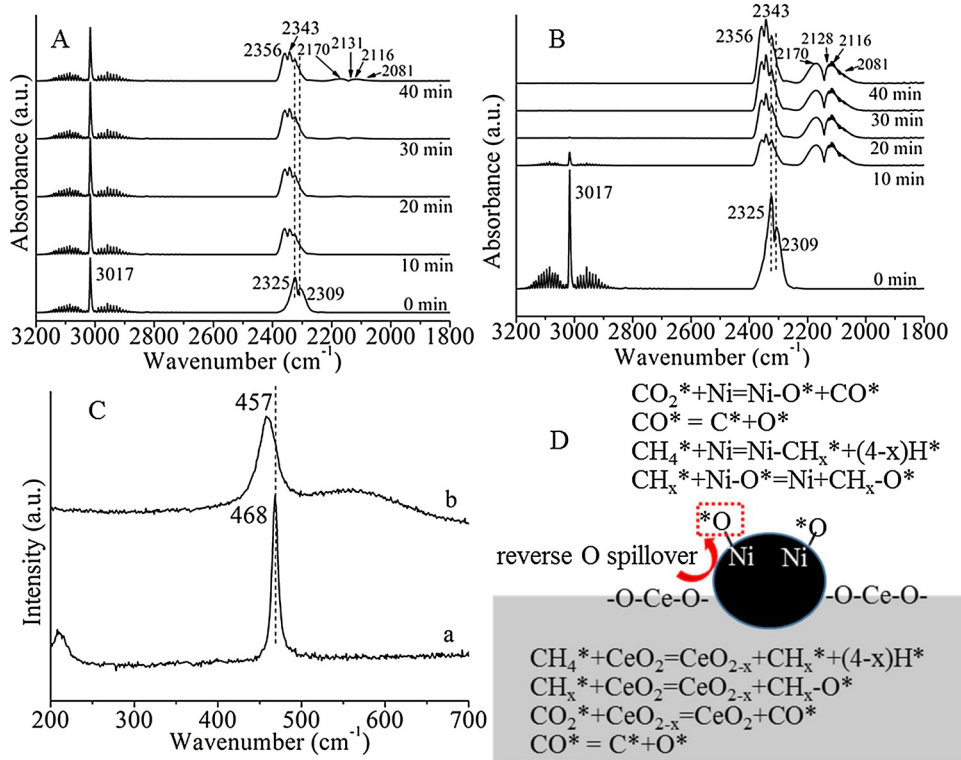


Fig. 5. In-situ FTIR spectra of the reactants and products from the reaction between ¹²C¹⁸O₂ and ¹²CH₄ on the samples of Ni/SiO₂ (A) and Ni/CeO₂ (B) at 700 °C and different times. Raman spectra of the fresh Ni/CeO₂ sample (a) and the used Ni/CeO₂ sample (b) after the reaction between ¹²C¹⁸O₂ and ¹²CH₄ at 700 °C for 40 min (C). Schematically illustrated synergistic effect among Ni nanoparticle and CeO₂ for CRM on Ni/CeO₂ (D).

for CRM. Is there synergistic effect among Ni nanocrystals and CeO₂ in Ni/CeO₂ that contributes to the good durability? To address the issue, we prepared a Ni/SiO₂ nanocomposite sample as SiO₂ as support has no catalytic activity for CRM. Ni/SiO₂ has an average Ni nanocrystal size of 24.1 nm (Fig. S6) and a BET surface area of 309.6 cm³ g⁻¹. We evaluated the catalytic activity of Ni/SiO₂ for CRM under the focalized UV-vis-IR illumination. In striking contrast to the good durability of Ni/CeO₂, the catalytic activity of Ni/SiO₂ rapidly decreases. After the

focalized illumination only for 8 h, its r_{CH_4} and r_{CO_2} values are reduced by 64.8% and 60.3%, respectively (Fig. 4B).

To affirm if the deactivation derives from the carbon deposition, after the durability tests, the used Ni/CeO₂ and Ni/SiO₂ samples were characterized by TG-MS. For the used Ni/CeO₂ sample, there is a weight loss of 54.12% from ~300 to 700 °C due to the carbon deposition during the 100 h durability test, which is verified by broad strong CO₂ peak owing to carbon combustion (Fig. 4C). The calculated rate of

carbon deposition (r_C) is 1.25×10^{-2} g g_{catal}⁻¹ h⁻¹, corresponding to 0.64% of the total reacted CH₄ converted to carbon. For the used Ni/SiO₂ sample, there is a weight loss of 63.75% from ~400 to 700 °C. This is ascribed to the carbon deposition during the 8 h durability test, evidenced by broad strong CO₂ peak due to carbon combustion (Fig. 4D). The calculated r_C value is 0.23 g g_{catal}⁻¹ h⁻¹, corresponding to 17.7% of the total reacted CH₄ converted to carbon. The results of TEM, HRTEM, and XRD also confirm that there is very severe deposition of graphite on the surface of Ni nanoparticles in Ni/SiO₂ as compared to Ni/CeO₂ (Figs S6–S8, and S1). This reveals the existence of a synergistic effect among Ni and CeO₂ nanoparticles in Ni/CeO₂ that significantly inhibits the carbon deposition as compared to Ni/SiO₂.

3.5. The origin of synergistic effect

To delve into the synergistic effect among Ni nanoparticles and CeO₂ in Ni/CeO₂, isotope labelling experiment was conducted for the reaction between ¹²C¹⁸O₂ and ¹²CH₄ on Ni/SiO₂ and Ni/CeO₂ at 700 °C (see Experimental). For Ni/SiO₂, when the reaction time increase to 10 min, the peaks of ¹²CH₄ at 3017 cm⁻¹ and the double peaks of ¹²C¹⁸O₂ around 2325 and 2309 cm⁻¹ are attenuated slightly (Fig. 5A), indicating that the reaction between ¹²CH₄ and ¹²C¹⁸O₂ proceeds slowly. There are two peaks at 2343 and 2322 cm⁻¹ observed. They are attributed the C–O stretching vibration of ¹²C¹⁸O¹⁶O (Fig. S9). With increasing the reaction time from 10 to 40 min, the peaks of ¹²C¹⁸O¹⁶O are intensified considerably. The formation of ¹²C¹⁸O¹⁶O is ascribed to the following reactions: 1) ¹²C¹⁸O₂ dissociates to ¹²C¹⁸O* and ¹⁸O* on the surface of Ni nanoparticles, and the produced ¹²C¹⁸O* is oxidized by ¹⁶O* chemisorbed on Ni nanoparticles formed in the process of the pre-reduction of Ni/SiO₂ in the flow of ¹²C¹⁶O₂ and ¹²CH₄ (see Experimental). 2) ¹²CH₄ dissociates to ¹²CH_x* species on the surface of Ni nanoparticles. The produced ¹²CH_x* (x = 0) is oxidized by ¹⁶O* or ¹⁸O* chemisorbed on Ni nanoparticles to produce ¹²C¹⁶O* or ¹²C¹⁸O*, which is subsequently oxidized by ¹⁸O* or ¹⁶O* chemisorbed on Ni nanoparticles to ¹²C¹⁸O¹⁶O*, respectively. However, only with increasing the reaction time to 40 min, are two weak peaks at 2170 and 2116 cm⁻¹ observed. They are attributed to the C–O stretching vibration of ¹²C¹⁶O (Fig. S9). No desorption of the produced ¹²C¹⁶O* or ¹²C¹⁸O* intermediates to gas phase before the reaction time of 30 min indicates that they mainly dissociate to ¹²C*. The formation of the C* species on the surface active sites of Ni nanoparticles due to the dissociation of both CO* and CH₄ to C* and their subsequent polymerization to graphite (Figs. S6–S8) inhibit the activation and dissociation of CO₂ and CH₄. This is evidenced by the rapid catalyst deactivation due to the severe carbon deposition even if CRM on Ni/SiO₂ only proceeded for 8 h (Fig. 4).

In striking contrast, for Ni/CeO₂, when the reaction time increase to 10 min, the C–H stretching vibration peaks of ¹²CH₄ around 3017 cm⁻¹ and the double strong peaks of ¹²C¹⁸O₂ around 2325 and 2309 cm⁻¹ are attenuated considerably (Fig. 5B), indicating that the reaction between ¹²CH₄ and ¹²C¹⁸O₂ proceeds rapidly. Four strong peaks at 2170, 2128, 2116, and 2081 cm⁻¹ are observed. The two peaks around 2128 and 2081 cm⁻¹ are assigned to the C–O stretching vibration of ¹²C¹⁸O [47]. The two peaks around 2170 and 2116 cm⁻¹ are attributed to the C–O stretching vibration of ¹²C¹⁶O (Fig. S9). Meanwhile, there are the double peaks at 2356 and 2343 cm⁻¹, which are assigned to the C–O stretching vibration modes of ¹²C¹⁶O₂ (Fig. S9). The production of ¹²C¹⁶O₂ is attributed to the further oxidation of the produced ¹²C¹⁶O* by ¹⁶O of CeO₂ in Ni/CeO₂ as well as by ¹⁶O* chemisorbed on Ni nanoparticles. Further increasing the reaction time leads to a disappearance of C–H stretching peak of ¹²CH₄ at 3017 cm⁻¹, indicating that ¹²CH₄ is almost completely reacted with ¹²C¹⁸O₂. The presence of ¹²C¹⁸O is due to the dissociation of ¹²C¹⁸O₂ to ¹⁸O* and ¹²C¹⁸O* as well as the reaction between the produced ¹⁸O* and ¹²CH_x* (x = 0) formed by the dissociation of ¹²CH₄. The presence of ¹²C¹⁶O is attributed to that the formed ¹²CH_x* (x = 0, here) and ¹²C*(formed by the dissociation of

¹²C¹⁸O*) are oxidized by ¹⁶O of CeO₂ in Ni/CeO₂ as well as by ¹⁶O* chemisorbed on Ni nanoparticles. The desorption of a considerable amount of ¹²C¹⁶O* and ¹²C¹⁸O* to gas phase even at the reaction time of 10 min indicates that their further dissociation to ¹²C* is significantly inhibited on Ni/CeO₂ due to the re-oxidation of the ¹²C* species to ¹²CO* by O of CeO₂ in Ni/CeO₂. This is evidenced by the good durability of Ni/CeO₂ due to its carbon deposition amount much lower than Ni/SiO₂ (Fig. 4).

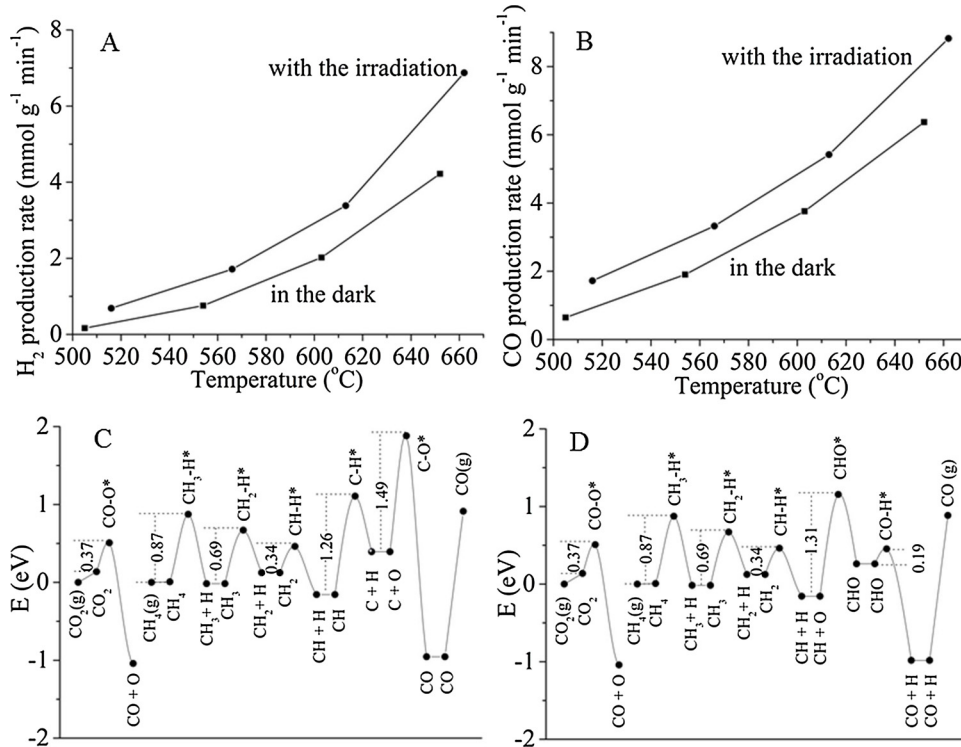
To further verify if O of CeO₂ in Ni/CeO₂ actually participates in the reaction between ¹²C¹⁸O₂ and ¹²CH₄, Raman was employed to characterize the fresh Ni/CeO₂ sample and the used Ni/CeO₂ sample after reaction between ¹²C¹⁸O₂ and ¹²CH₄ on Ni/CeO₂ at 700 °C for 40 min. The fresh Ni/CeO₂ sample has a strong Raman peak located at 468 cm⁻¹ (Fig. 5C), which is assigned to the F_{2g} mode of Ce–¹⁶O stretching [48,49]. Compared to that of the fresh Ni/CeO₂ sample, the Ce–O stretching peak of the used Ni/CeO₂ sample shifts to a lower wavenumber of 457 cm⁻¹. The isotope shift clearly indicates the formation of Ce–¹⁸O bonds after the reaction between ¹²C¹⁸O₂ and ¹²CH₄ on Ni/CeO₂. The Ce–¹⁸O bond formation is due to the reactions as follows: ¹⁶O vacancies of ceria in Ni/CeO₂ are formed due to the oxidation of the CH_x species (generated by the dissociation of CH₄) by ¹⁶O of CeO₂ in Ni/CeO₂ as well as the migration of ¹⁶O of CeO₂ at the Ni/CeO₂ interface via the reverse oxygen spillover to Ni nanoparticles at high reaction temperature [50]. The formation of O vacancies of ceria is confirmed by the observation that compared to that of the fresh Ni/CeO₂ sample, the used Ni/CeO₂ sample has a new broad peak centered at 570 cm⁻¹, which is attributable to a Frenkel-type oxygen defect-induced mode of ceria [48,49]. The ¹⁶O vacancies of ceria in Ni/CeO₂ are replenished by ¹⁸O* formed by the dissociation of ¹²C¹⁸O₂ molecules on the ¹⁶O vacancies. The migration of ¹⁶O of CeO₂ at the Ni/CeO₂ interface to Ni nanoparticles accelerates the oxidation of the *C species formed on Ni nanoparticles, thus inhibiting the accumulation and subsequent graphitization of the *C species. The isotope labeling results undoubtedly reveals that the lattice oxygen of CeO₂ in Ni/CeO₂ participates in the oxidation of the C* species formed on Ni nanoparticles through the migration at the Ni/CeO₂ interface, thus significantly improving the catalytic stability due to the inhibition of carbon deposition as schematically illustrated in Fig. 5D.

3.6. Photoactivation

In order to clarify if the excellent catalytic activity (Fig. 3) originates merely from solar-light-driven thermocatalytic CRM, we measured the catalytic activity of Ni/CeO₂ for CRM with the focused UV-vis-IR irradiation and in the dark at different temperatures in the same reactor under otherwise identical reaction conditions (see Experimental). At the same reaction temperature above 500 °C, compared to that in the dark, H₂ production rate and CO production rate of Ni/CeO₂ are considerably improved under the focused UV-vis-IR irradiation (Fig. 6A and B). As shown in Fig. 3B, Ni/CeO₂ has no photocatalytic activity under the UV-vis-IR irradiation although CeO₂

is an n-type semiconductor photocatalyst. The significant increase in the catalytic activity upon the focused UV-vis-IR irradiation at temperatures above 500 °C indicates the presence of a novel photoactivation effect besides the solar-light-driven thermocatalysis. Obviously, the novel photoactivation is quite different from conventional photocatalysis of redox reaction triggered by photogenerated holes and electrons on semiconductor photocatalysts (e.g., TiO₂).

In order to put insight into the novel photoactivation, we made theoretic investigation in the effect of the irradiation on the catalytic activity of Ni/CeO₂ for CRM by DFT calculations. As discussed in Section 2.2 and as shown in Fig. 2A and B, the excellent catalytic activity of Ni/CeO₂ under the focused irradiation mainly arises from the important role of Ni nanocrystals. To simplify the DFT calculation, we merely consider the effect of the irradiation on the catalytic activity of Ni nanocrystals in Ni/CeO₂. The reaction pathways of CRM on metallic



Ni involve elemental steps of CO_2 dissociation to produce CO and O , CH_4 dissociation to produce CH_x ($x = 0 \sim 3$) and H , and oxidation of CH_x by O . The comprehensive DFT investigation reported indicates that the dominant steps are the CH and C oxidations [51,52]. We calculated activation energies (E_a) of the elementary steps of CRM on a Ni_{36} slab with {111} surface in the ground state (in the dark) and the excited state (with the irradiation). Upon the absorption of the irradiation (Fig. 3A), metallic Ni is promoted to its excited state via the excitation of d electrons. To calculate E_a values of the elementary steps on the Ni_{36} slab in the excited state, we utilized a constrained occupancy approach by setting the exciting two d electrons of the 36 Ni atoms in the Ni_{36} slab to the excited state through changing the number of electrons in the up and down spin configurations of the Ni_{36} slab [53,54]. As can be seen from Figs. 6C, D, and S10, the E_a values of the dissociation of CH_4 , CH_3 , CH_2 , CO_2 , and CHO in the excited states are 0.87, 0.69, 0.34, 0.37, and 0.19 eV, respectively. They are almost identical to the corresponding values in ground states (0.87, 0.69, 0.35, 0.42, and 0.21 eV) [31,51]. The result indicates that the irradiation does not affect the activation of the dissociation of CH_4 , CH_3 , CH_2 , CO_2 , and CHO . In striking contrast, the E_a values of the CH dissociation and the oxidations of C and CH in the excited state (1.26, 1.49, 1.31 eV) are obviously lower than the corresponding values in the ground states (1.37, 1.61, 1.43 eV). This result indicates that the irradiation accelerates the activation of the CH dissociation and the oxidations of C and CH . The acceleration of the dominant steps of the C and CH oxidations for CRM on metallic Ni upon the irradiation results in the considerable increase in the catalytic activity as shown in Fig. 6A and B.

4. Conclusions

In conclusion, a Ni/CeO_2 nanocomposite was prepared by a facile method. The Ni/CeO_2 nanocomposite owns good catalytic activity and stability for CRM with focalized UV-vis-IR and Vis-IR illumination. It generates massive production rates of H_2 and CO with high solar-to-fuel efficiencies. The effective catalytic activity of Ni/CeO_2 derives from the SLD thermocatalytic CRM because of its efficient thermocatalytic activity and photothermal conversion due to its strong absorption across

Fig. 6. H_2 production rate (A) and CO production rate (B) of Ni/CeO_2 for CRM with the focused irradiation and in the dark at different temperatures. Relative free energies of CMR elementary steps through the pathways of C oxidation (C) and CH oxidation (D) on a Ni_{36} slab in the excited state calculated by DFT, where * represents the corresponding transition states.

the whole solar spectra. It is found that a synergistic effect among Ni nanoparticles and CeO_2 exists for CRM on Ni/CeO_2 : The lattice oxygen of CeO_2 in Ni/CeO_2 participates in the oxidation of carbon species formed on Ni nanoparticles via the migration at the Ni/CeO_2 interface, thus significantly improving the catalytic stability owing to carbon deposition inhibition. A novel photoactivation is found to considerably improve the solar-light-driven thermocatalytic activity of Ni/CeO_2 . We put insight into the novel photoactivation by DFT calculation: The irradiation obviously decreases the activation energy of the dominant steps of the C and CH oxidations for CRM on metallic Ni. The present work provides an effective and promising strategy of converting GHS to fuels and solar energy to chemical energy.

Acknowledgements

This work was supported by National Natural Science Foundation of China (21673168, 21473127). Q. Zhang and Dr. M. Y. Mao have same contribution to the paper.

Appendix A. Supplementary data

Supplementary material related to this article can be found, in the online version, at doi:<https://doi.org/10.1016/j.apcatb.2018.08.052>.

References

- [1] W.C. Chueh, C. Falter, M. Abbott, D. Scipio, P. Furler, S.M. Haile, A. Steinfield, *Science* 330 (2010) 1797–1801.
- [2] D. Marxer, P. Furler, M. Takacs, A. Steinfield, *Energy Environ. Sci.* 10 (2017) 1142–1149.
- [3] X.Q. An, K.F. Li, J.W. Tang, *ChemSusChem* 7 (2014) 1086–1093.
- [4] Y.F. Zhao, G.B. Chen, T. Bian, C. Zhou, G.I.N. Waterhouse, L.Z. Wu, C.H. Tung, L.J. Smith, D. O'Hare, T.R. Zhang, *Adv. Mater.* 27 (2015) 7824–7831.
- [5] F. Raziq, Y. Qu, M. Humayun, A. Zada, H.T. Yu, L.Q. Jing, *Appl. Catal. B* 201 (2017) 486–494.
- [6] J.S. Wang, C.L. Qin, H.J. Wang, M.N. Chu, A. Zada, X.L. Zhang, J.D. Li, F. Raziq, Y. Qu, L.Q. Jing, *Appl. Catal. B* 221 (2018) 459–466.
- [7] L. Yuan, C. Han, M. Pagliaro, Y.J. Xu, *J. Phys. Chem. C* 120 (2016) 265–273.
- [8] S.W. Cao, B.J. Shen, T. Tong, J.W. Fu, J.G. Yu, *Adv. Funct. Mater.* 28 (2018)

- 1800136.
- [9] G. Yang, D.M. Chen, H. Ding, J.J. Feng, J.Z. Zhang, Y.F. Zhu, S. Hamid, D.W. Bahnmann, *Appl. Catal. B* 219 (2017) 611–618.
- [10] Y. Wang, L.N. Zhang, X.Y. Zhang, Z.Z. Zhang, Y.C. Tong, F.Y. Li, J.C.S. Wu b, X.X. Wang, *Appl. Catal. B* 206 (2017) 158–167.
- [11] S.Y. Zhu, S.J. Liang, Y. Wang, X.Y. Zhang, F.Y. Li, H.X. Lin, Z.Z. Zhang, X.X. Wang, *Appl. Catal. B* 187 (2016) 11–18.
- [12] L. Lu, B. Wang, S.M. Wang, Z. Shi, S.C. Yan, Z.G. Zou, *Adv. Funct. Mater.* 27 (2017) 1702447.
- [13] X.J. Wang, X.L. Zhao, D.Q. Zhang, G.S. Li, H.X. Li, *Appl. Catal. B* 228 (2018) 47–53.
- [14] J. Qin, S.B. Wang, X.C. Wang, *Appl. Catal. B* 209 (2017) 476–482.
- [15] S.B. Wang, X.C. Wang, Imidazolium ionic liquids, *Angew. Chem. Int. Ed.* 55 (2016) 2308–2320.
- [16] Q.G. Zhai, S.J. Xie, W.Q. Fan, Q.H. Zhang, Y. Wang, W.P. Deng, Y. Wang, *Angew. Chem.* 125 (2013) 5888–5891.
- [17] J.N. Qin, S.B. Wang, X.C. Wang, *Appl. Catal. B* 209 (2017) 476–482.
- [18] U. Kang, S.K. Choi, D.J. Ham, S.M. Ji, W.Y. Choi, D.S. Han, A. Abdel-Wahab, H. Park, *Energy Environ. Sci.* 8 (2015) 2638–2643.
- [19] W.N. Wang, W.J. An, B. Ramalingam, S. Mukherjee, D.M. Niedzwiedzki, S. Gangopadhyay, P. Biswas, *J. Am. Chem. Soc.* 134 (2012) 11276–11281.
- [20] H.W. Huang, J.J. Lin, G.B. Zhu, Y.X. Weng, X.X. Wang, X.Z. Fu, J.L. Long, *Angew. Chem. Int. Ed.* 55 (2016) 8314–8318.
- [21] P.G. O'Brien, A. Sandhel, T.E. Wood, A.A. Jelle, L.B. Hoch, D.D. Perovic, C.A. Mims, G.A. Ozin, *Adv. Sci.* 1 (2014) 1400001.
- [22] L.B. Hoch, P.G. O'Brien, A. Jelle, A. Sandhel, D.D. Perovic, C.A. Mims, G.A. Ozin, *ACS Nano* 10 (2016) 9017–9025.
- [23] L. Yuliati, H. Yoshida, *Chem. Soc. Rev.* 37 (2008) 1592–1602.
- [24] G. Mahmodi, S. Sharifnia, M. Madani, V. Vatanpour, *Sol. Energy* 97 (2013) 186–194.
- [25] D.S.A. Simakov, M.M. Wright, S. Ahmed, E.M.A. Mokheimer, Y. Roman-Leshkov, *Catal. Sci. Technol.* 5 (2015) 1991–2016.
- [26] (a) T. Kodama, A. Kiyama, K.I. Shimizu, *Energy Fuels* 17 (2003) 13–17; (b) T. Kodama, H. Ohtake, K.I. Shimizu, Y. Kitayama, *Energy Fuels* 16 (2002) 1016–1023.
- [27] C. Agrafiotis, H. von Storch, M. Roeb, C. Sattler, *Renew. Sustain. Energy Rev.* 29 (2014) 656–682.
- [28] J.K. Dahl, A.W. Weimer, A. Lewandowski, C. Bingham, F. Bruetsch, A. Steinfeld, *Ind. Eng. Chem. Res.* 43 (2004) 5489–5495.
- [29] B. Han, W. Wei, L. Chang, P.F. Cheng, Y.H. Hu, *ACS Catal.* 6 (2016) 494–497.
- [30] H.M. Liu, X.G. Meng, T.D. Dao, H.B. Zhang, P. Li, K. Chang, T. Wang, M. Li, T. Nagao, J.H. Ye, *Angew. Chem. Int. Ed.* 54 (2015) 11545–11549.
- [31] (a) H. Huang, M.Y. Mao, Q. Zhang, Y.Z. Li, J.L. Bai, Y. Yang, M. Zeng, X.J. Zhao, *Adv. Energy Mater.* (2018) 1702472; (b) M.Y. Mao, Q. Zhang, Y. Yang, Y.Z. Li, H. Huang, Z.K. Jiang, Q.Q. Hu, X.J. Zhao, *Green Chem.* 20 (2018) 2857–2869.
- [32] H.M. Liu, T.D. Dao, L.Q. Liu, X.G. Meng, T. Nagao, J.H. Ye, *Appl. Catal. B* 209 (2017) 183–189.
- [33] Y. Sun, T. Ritchie, S.S. Hla, S. McEvoy, W. Stein, J.H. Edwards, *J. Nat. Gas Chem.* 20 (2011) 568–576.
- [34] N. Sun, X. Wen, F. Wang, W. Wei, Y. Sun, *Energy Environ. Sci.* 3 (2010) 366–369.
- [35] D. Pakhare, J. Spivey, *Chem. Soc. Rev.* 43 (2014) 7813–7837.
- [36] J.T. Hou, Y.Z. Li, M.Y. Mao, Y.Z. Yue, G.N. Greaves, X.J. Zhao, *Nanoscale* 7 (2015) 2633–2640.
- [37] G. Kresse, D. Joubert, *Phys. Rev. B* 59 (1999) 1758.
- [38] G. Kresse, J. Hafner, *Phys. Rev. B* 48 (1993) 13115.
- [39] G. Henkelman, H. Jonsson, *J. Chem. Phys.* 111 (1999) 7010.
- [40] D. Sheppard, R. Terrell, G. Henkelman, *J. Chem. Phys.* 128 (2008) 10.
- [41] C.D. Wagner, W.M. Riggs, L.E. Davis, *Handbook of X-ray Photoelectron Spectroscopy*, PerkinElmer, Waltham, MA, 1979, p. 80.
- [42] M. Zeng, Y.Z. Li, M.Y. Mao, J.L. Bai, L. Ren, X.J. Zhao, *ACS Catal.* 5 (2015) 3278–3286.
- [43] M.J. Munoz-Batista, M.N. Gomez-Cerezo, A. Kubacka, D. Tudela, M. Fernandez-Garcia, *ACS Catal.* 4 (2014) 63–72.
- [44] Y.Z. Li, Q. Sun, M. Kong, W.Q. Shi, J.C. Huang, J.W. Tang, X.J. Zhao, *J. Phys. Chem. C* 115 (2011) 14050–14057.
- [45] A.D. Liyanage, S.D. Perera, K. Tan, Y. Chabal, K.J. Balkus Jr, *ACS Catal.* 4 (2014) 577–584.
- [46] D.A. Perry, R.L. Borchers, J.W. Golden, A.R. Owen, A.S. Price, W.A. Henry, F. Watanabe, A.S. Biris, *J. Phys. Chem. Lett.* 4 (2013) 3945–3949.
- [47] B.S. Shete, V.S. Kamble, N.M. Gupta, V.B. Kartha, *Phys. Chem. Chem. Phys.* 1 (1999) 191–198.
- [48] W.Q. Shi, Y.Z. Li, J.T. Hou, H.Q. Lv, X.J. Zhao, P.F. Fang, F. Zheng, S.J. Wang, *J. Mater. Chem. A* 1 (2013) 728–734.
- [49] Y.J. Lee, G.H. He, A.J. Akey, R. Si, M. Flytzani-Stephanopoulos, I.P. Herman, *J. Am. Chem. Soc.* 133 (2011) 12952–12955.
- [50] M.Y. Mao, H.Q. Lv, Y.Z. Li, Y. Yang, M. Zeng, N. Li, X.J. Zhao, *ACS Catal.* 6 (2016) 418–427.
- [51] Y.A. Zhu, D. Chen, X.G. Zhou, W.K. Yuan, *Catal. Today* 148 (2009) 260–267.
- [52] Z.Y. Wang, X.M. Cao, J.H. Zhu, P. Hu, *J. Catal.* 311 (2014) 469.
- [53] A. Canning, A. Chaudhry, R. Boutchko, N. Gronbeck-Jensen, *Phys. Rev. B* 83 (2011) 125115.
- [54] F. Liu, M. Zeng, Y.Z. Li, Y. Yang, M.Y. Mao, X.J. Zhao, *Adv. Funct. Mater.* 26 (2016) 4518.